Full length article

Boron doped ultrastrong and ductile high-entropy alloys

Jae Bok Seol [a], [1], Jae Wung Bae [b], [1], Zhiming Li [c], Jong Chan Han [d], Jung Gi Kim [b], Dierk Raabe [c], [*], Hyoung Seop Kim [b], [**]

[a] National Institute of Nanomaterials Technology, Center for High Entropy Alloys, POSTECH, Pohang, 37673, South Korea
[b] Department of Materials Science and Engineering, Center for High-Entropy Alloys, POSTECH, Pohang, 37673, South Korea
[c] Max-Planck-Institut für Eisenforschung, Max-Planck-Straße 1, D-40237, Düsseldorf, Germany
[d] Department of Materials Science and Engineering, POSTECH, Pohang, 37673, South Korea

ARTICLE INFO

ABSTRACT

A new class of materials called high-entropy alloys (HEAs) constitutes multiple principal elements in similar compositional fractions. The equiatomic $Fe_{20}Mn_{20}Cr_{20}Co_{20}Ni_{20}$ (at%) HEA shows attractive mechanical properties, particularly under cryogenic conditions. Yet, it lacks sufficient yield and ultimate tensile strengths at room temperature. To strengthen these materials, various strategies have been proposed mainly by tuning the composition of the bulk material while no efforts have been made to decorate and strengthen the grain boundaries. Here, we introduce a new HEA design approach that is based on compositionally conditioning the grain boundaries instead of the bulk. We found that as little as 30 ppm of boron doping in single-phase HEAs, more specific in an equiatomic FeMnCrCoNi and in a non-equiatomic $Fe_{40}Mn_{40}Cr_{10}Co_{10}$ (at%), improves dramatically their mechanical properties, increasing their yield strength by more than 100% and ultimate tensile strength by ~40% at comparable or even better ductility. Boron decorates the grain boundaries and acts twofold, through interface strengthening and grain size reduction. These effects enhance grain boundary cohesion and retard capillary driven grain coarsening, thereby qualifying boron-induced grain boundary engineering as an ideal strategy for the development of advanced HEAs.

© 2018 Acta Materialia Inc. Published by Elsevier Ltd. All rights reserved.

1. Introduction

High-entropy alloys (HEAs), comprising multiple principal elements, have drawn much interest due to their attractive mechanical response [1—10]. In contrast to traditional metal alloys that are typically based on one or two primary elements, several properties of HEAs were originally attributed to entropy-driven phase stability resulting in entropy maximization as a governing design rule [4,5]. A subsidiary design strategy based on phase metastability [11—13] enables the development of dual-phase $Fe_{50}Mn_{30}Cr_{10}Co_{10}$ (at%) non-equiatomic HEAs with high strain-hardening owing to the activation of athermal deformation mechanisms that are activated under load. This, in turn, leads to the highest ductility reported so far for strong HEAs at room temperature [13].

An alternative method of strengthening HEAs involves exploiting precipitation strengthening through formation of secondary precipitates in a matrix phase [14—17]. Through such a compositional modification, the room-temperature yield and tensile strength values of precipitation strengthened HEAs with appreciableductility (<30%) have been found to exceed 800 MPa and 1.0 GPa, respectively. However, despite such progress, the foregoing strategies suggest that there are still unresolved effects in the utilization of such bulk compositional tuning measures towards either enhanced phase stability or metastability, also when using additional precipitation strengthening. The lack of sufficient room-temperature strengths at enhanced ductility ranges (>30%) is a point of high interest for structural applications of HEAs. For instance, strength values of bulk compositionally tuned HEAs still remain below those of most high-strength steels. Hence, further modification of the bulk composition of HEAs alone fails to utilize all available microstructure design windows and leaves the issue of grain coarsening during thermomechanical processing unresolved. To date, no experimental attempts have been reported to investigate how solute decoration in HEAs can be used to manipulate grain boundary characteristics and consequently the mechanical

* Corresponding author.
** Corresponding author.
  E-mail addresses: d.raabe@mpie.de (D. Raabe), hskim@postech.ac.kr (H.S. Kim).
[1] These authors contributed equally to this work.

response.

Here, we propose a new strategy for overcoming the aforementioned limitations of other recently developed HEAs, namely, through compositional modification of the grain boundaries instead of the bulk. The proposed strategy involves selection of a face-centred cubic (fcc) single-phase equiatomic $Fe_{20}Mn_{20}Cr_{20}Co_{20}Ni_{20}$ (at%) alloy and a non-equiatomic $Fe_{40}Mn_{40}Cr_{10}Co_{10}$ (at%) alloy [18], and doping them with 30 ppm (by weight) of boron. Driven by the Gibbsian reduction in grain boundary (GB) energy, the boron then segregates to the interfaces in polycrystalline materials. This effect triggers microstructure manipulation twofold. Firstly, it enhances the load-bearing capacity of individual interfaces through an increase in GB cohesion [19–26], thereby reducing the probability of occurrence of catastrophic interface failure in structural components. Secondly, the interface solute decoration and the reduced GB energy introduce an enhanced GB drag effect and a reduced Gibbs-Thomson force during recrystallization of polycrystalline materials and capillary-driven grain coarsening, leading to grain-refinement during heat treatment compared to undoped HEAs. The associated Hall-Petch effect enhances both, strength and ductility of the materials.

From a practical perspective boron doping offers two more advantages – it is more efficient to alloy the grain boundaries only instead of the entire bulk material. Secondly, improving the mechanical properties through inexpensive GB dopants is more preferable over the use of expensive alloying elements, such as Ni, Co, and Cr, for further bulk compositional tuning.

Boron has been used successfully as a dopant in metallurgy, conveying beneficial compositional effects to interfaces of polycrystalline materials [19–26]. The segregation engineering concept proposed in this work is based on boron's well-known effect on interfaces. Various studies reported that boron segregation leads to changes in the GB structure, energy, composition, and properties, yielding improved mechanical behavior [26]. When doped with an amount below a critical level of ≤ 50 ppm (by weight), boron tends to preferentially decorate random high-angle GBs upon moderate diffusion heating. However, care must be exercised while applying this effect. Beyond a certain critical doping level, the use of boron may turn harmful leading to weakening of the GBs through formation of brittle compounds that contain boron. Hence, additional efforts have been made in this study on identifying the most beneficial amount of boron in the equiatomic $Fe_{20}Mn_{20}Cr_{20}Co_{20}Ni_{20}$ HEA by changing doping concentrations in the range between 30 and 300 ppm (by weight).

2. Experimental

The near-equiatomic $Fe_{20}Mn_{20}Cr_{20}Co_{20}Ni_{20}$ (at%) HEA systems and their boron-doped versions were cast in a vacuum induction furnace (MC100V, Indutherm, Walzbachtal-Wossingen, Germany) using pure metals (purity higher than 99.9 wt%) for the undoped samples and a high-purity FeB lump for the boron-doped HEA samples. Casting was performed under Ar protective atmosphere. The obtained rectangular ingots with dimensions of $100 \times 35 \times 8$ mm^3 were homogenized at 1100 °C for 360 min, pickled in a 20% HCl solution, and milled to a thickness of 7 mm. Further grain refinement was achieved through cold-rolling to a thickness reduction ratio of 75% (the thickness changed from 7 to 1.5 mm). For recrystallization of boron-doped (30–300 ppm by weight) and undoped samples, the rolled sheets were annealed at a temperature of 800 °C for 60 min and subsequently quenched in water. Hereafter, all specimens with boron-doped compositions are given by weight per cent unless specified otherwise. In particular, samples doped with 30-ppm-boron were annealed at temperatures in the range between 650 and 1100 °C for 60 min. A schematic of
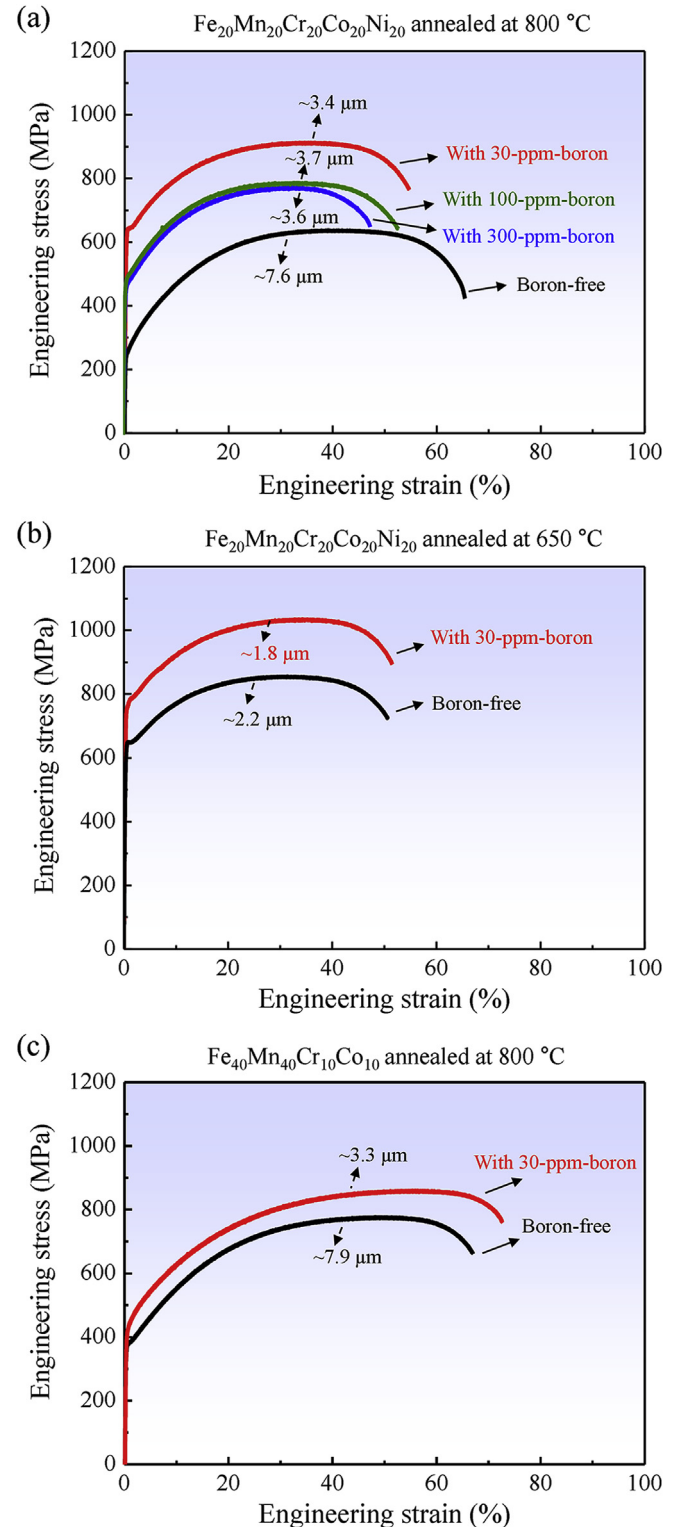

Fig. 1. Room-temperature mechanical response of boron-doped (30 ppm, red) and undoped (black) single-phase HEAs in the recrystallized state: (a) boron-doped and undoped FeMnCrCoNi equiatomic samples annealed at 800 °C; (b) boron-doped and undoped equiatomic samples subjected to annealing at 650 °C; (c) boron-doped and undoped FeMnCrCo non-equiatomic samples subjected to annealing at 800 °C. Also included in (a) are the tensile properties of the equiatomic samples with different boron concentrations (100 ppm, green; 300 ppm, blue). Grain sizes (dotted arrows) of all recrystallized samples are in micrometres. HEA, high-entropy alloy. (For interpretation of the references to color in this figure legend, the reader is referred to the Web version of this article.)

these thermomechanical processes is given in Supplementary Information Fig. S1. To study boron doping also on single-phase non-equiatomic HEAs, we synthesized boron-free and boron-doped (30 ppm) $Fe_{40}Mn_{40}Cr_{10}Co_{10}$ (at%) HEAs through the same processing, followed by 800 °C annealing for 60 min. As demonstrated by microstructure characterization using X-ray diffraction (XRD), both, boron-doped and undoped HEAs possess single fcc phase structure in all grain-refined, viz. recrystallized states, Supplementary Information Fig. S2.

Flat specimens with a gauge length of 6.4 mm, a gauge width of 2.5 mm, and a thickness of 1.5 mm were cut from a quarter through-thickness position of the annealed samples for tensile testing. A schematic illustration of the tensile specimens is provided in Supplementary Information Fig. S3. All samples used in the tensile tests were prepared along the longitudinal direction. The mechanical properties of the boron-doped (30–300 ppm) and undoped $Fe_{20}Mn_{20}Cr_{20}Co_{20}Ni_{20}$ specimens subjected to thermal annealing between 650 and 800 °C for 60 min were tested under uniaxial tension in an Instron Model 5582 test frame (Instron Corp, Canton, MA, USA). The boron-doped and undoped $Fe_{40}Mn_{40}Cr_{10}Co_{10}$ samples were also tensile-tested. For all tensile tests, a 100-kN load cell, operated at a strain rate of 10^{-3} s^{-1}, was used at room temperature. The evolution of the local strain levels during tensile testing was determined by the digital image correlation (DIC) method. Three samples were tensile-tested for each condition to confirm reproducibility, and representative data are shown.

Multiple characterization techniques were used to analyse the microstructures of the annealed and recrystallized near-equiatomic and non-equiatomic HEA samples. For observation of the boron-induced grain refinement in the annealed HEA samples, electron backscatter diffraction (EBSD) analysis was performed using a field-emission scanning electron microscopy (FE-SEM) system (Quanta 3d FEG, FEI Company, USA) equipped with an OPTIMUSTM transmission Kikuchi diffraction (TKD, e-Flash^{HR}, ARGUSTM electron detection system, Bruker, Germany). The EBSD data were interpreted using the TSL OIM data collection software (TSL OIM Analysis 7). Based on the general description that recrystallized grains have a grain orientation spread (GOS) value < 2° [27], we determined the area fraction of recrystallized grains in both, boron-free
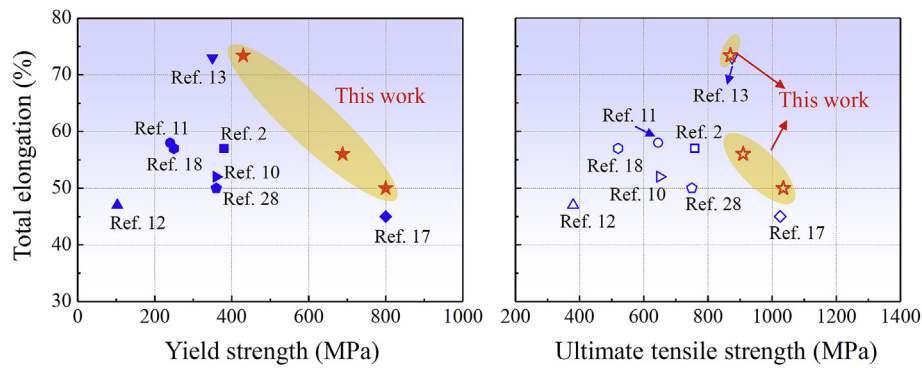
Fig. 2. Comparison of the YS (filled symbols) and of the UTS (open symbols) versus TE obtained in this work (30 ppm-boron case; stars) with other recently developed HEAs [2,10–13,17,18,28]. The YS and UTS values of the reference alloys with total tensile elongation <30% are not shown for comparison. YS, yield strength; UTS, ultimate tensile strength; TE, total elongation.
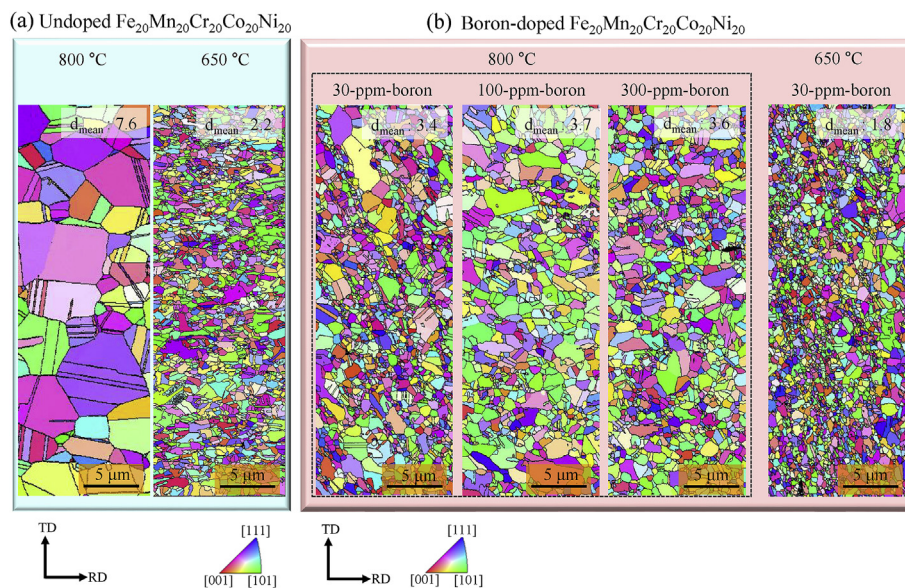
Fig. 3. Typical EBSD grain maps of the recrystallized $Fe_{20}Mn_{20}Cr_{20}Co_{20}Ni_{20}$ HEAs subject to anneals at 800 and 650 °C: (a) undoped samples; (b) boron-doped samples with different boron concentrations. The values of mean grain sizes d_{mean} of all recrystallized samples are in micrometres. To determine the grain size from the EBSD data using a conventional mean-linear-intercept method, high angle grain boundaries with a misorientation angle $\geq 15°$ were defined as grain boundaries. The annealing twin boundaries were excluded from the grain size measurement, i.e. they were not counted as grain boundaries. EBSD: electron backscatter diffraction.
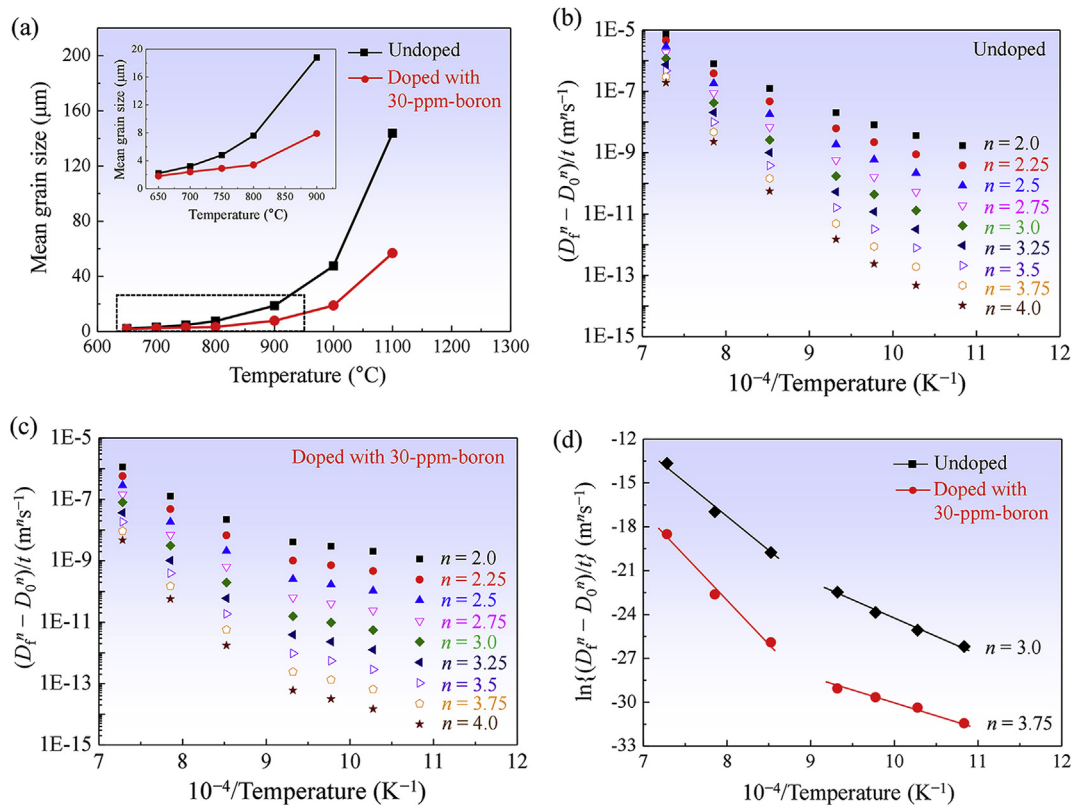
and boron-doped $Fe_{20}Mn_{20}Cr_{20}Co_{20}Ni_{20}$ HEA samples subjected to annealing at temperatures of 650–800 °C for 60 min. For this purpose, a large number of EBSD scans with the same probed analysis area of $1177 \times 182 \, \mu m^2$ were performed on the transverse plane of each sample. From these EBSD maps the GOS measure was determined. Atom probe tomography (APT) tips were prepared using a focused ion beam (FIB) milling system (FEI Helios Nanolab 650i) from regions of interest containing high-angle GBs detected through a prior EBSD scan. To characterize the GBs, as primarily targeted in this work, APT tips were observed through transmission electron microscopy (TEM) and high-resolution (HR) TEM prior to APT analysis. Bright-field low-magnification TEM images, selected area diffraction pattern (SADP), and HRTEM lattice images were obtained using a JEOL 2010F analytical TEM system equipped with an aberration corrector. The system was operated at an acceleration voltage of 200 kV. The TEM-probed APT tips were re-sharpened using a FIB instrument until the undesired electron-damage layers on the tip surface were removed, and subsequently, the chemical composition of boron at the GBs was investigated using APT analysis (LEAP 4000X HR, Cameca Inc.) at the atomic scale. All measurements were performed in the voltage-pulsing mode at a detection rate of 0.2%; pulse fraction of 20%; and pulse repetition rate of 200 kHz. All measurements were performed at 60 K under a pressure below 10^{-7} Pa. Deformation structures of the tensile-tested $Fe_{20}Mn_{20}Cr_{20}Co_{20}Ni_{20}$ and $Fe_{40}Mn_{40}Cr_{10}Co_{10}$ samples were analysed using a combined analysis involving TKD or EBSD with TEM or HRTEM. The TKD data were interpreted using the Bruker EBSD software.

3. Results

3.1. Mechanical properties

Fig. 1 shows the room-temperature mechanical response of various boron-doped and undoped equiatomic $Fe_{20}Mn_{20}Cr_{20}Co_{20}Ni_{20}$ samples subjected to annealing at 800 °C for 60 min (Fig. 1(a)), and boron-doped (30 ppm) samples subjected to annealing at 650 °C for 60 min (Fig. 1(b)). Also included are the non-equiatomic $Fe_{40}Mn_{40}Cr_{10}Co_{10}$ samples annealed at 800 °C for 60 min, Fig. 1(c). The yield strength (YS) and ultimate tensile strength (UTS) of all boron-doped HEAs exceed those of their undoped counterparts subjected to the same processing routes, while the total elongation (TE) did not show substantial changes. Interestingly, boron doping with 30 ppm provides the most robust properties amongst the equiatomic $Fe_{20}Mn_{20}Cr_{20}Co_{20}Ni_{20}$ samples (Fig. 1(a)). The grain sizes (dotted arrows) of all recrystallized samples were in micrometres, as determined from EBSD analyses.

To underline the profound improvement in tensile properties brought about by boron doping, specifically for the 30 ppm case, the YS, UTS and TE of other recently developed HEA systems [2,10–13,17,18,28] are also shown in Fig. 2. This result shows that for both, the equiatomic FeMnCrCoNi and the non-equiatomic $Fe_{40}Mn_{40}Cr_{10}Co_{10}$ HEAs, GB segregation engineering by boron doping with 30 ppm yields a YS value of approx. 800 MPa (for equiatomic FeMnCrCoNi annealed at 650 °C), 630 MPa (for equiatomic FeMnCrCoNi annealed at 800 °C), and 450 MPa (for non-equiatomic FeMnCrCo annealed at 800 °C). The alloy reached UTS values of 1040 MPa (for equiatomic FeMnCrCoNi annealed at

Fig. 4. (a) Variation in mean grain size of the boron-doped (30 ppm, red) and undoped (black) equiatomic $Fe_{20}Mn_{20}Cr_{20}Co_{20}Ni_{20}$ HEAs in the recrystallized state, determined from EBSD, as a function of annealing temperatures at an annealing time of 60 min. Inset is an enlarged view of the curve revealing an order of magnitude difference in grain size between the doped and undoped HEAs. Plot of $(D_f^n - D_0^n)/t$, where D is the grain size, n is the grain growth exponent, and t is the time, against the reciprocal of the annealing temperature as a function of the values of grain growth exponent n: (b) undoped samples; (c) boron-doped samples. By changing the values of the grain growth exponent n from 2 to 4, the data points in (b) and (c) were fitted. (d) Activation energy of fcc grain growth for the boron-doped (30 ppm, red) and undoped (black) equiatomic $Fe_{20}Mn_{20}Cr_{20}Co_{20}Ni_{20}$ HEAs in the recrystallized state. (For interpretation of the references to color in this figure legend, the reader is referred to the Web version of this article.)

650 °C), 920 MPa (for equiatomic FeMnCrCoNi annealed at 800 °C), 880 MPa (for non-equiatomic FeMnCrCo annealed at 800 °C), respectively, and TE of 57% (for equiatomic FeMnCrCoNi annealed at 650 °C), 52% (for equiatomic FeMnCrCoNi annealed at 800 °C), 73% (for the non-equiatomic FeMnCrCo annealed at 800 °C) at room temperature, exceeding the corresponding property values of the undoped alloys. This result confirms that compositional modification of GBs instead of the bulk material through doping with very small quantities (30 ppm) of boron is an efficient method for attaining better mechanical properties of single-phase HEAs at room temperature.

3.2. Microstructural characterization

3.2.1. Grain size variation and texture change via boron doping

The mean grain sizes of all equiatomic $Fe_{20}Mn_{20}Cr_{20}Co_{20}Ni_{20}$

samples (i.e. with and without boron) in the recrystallized state (i.e. 800 and 650 °C for 60 min) were determined from EBSD maps, Fig. 3. For conciseness, the EBSD results of the samples annealed at all the different temperatures were not shown here.

In particular, the mean grain sizes of the $Fe_{20}Mn_{20}Cr_{20}Co_{20}Ni_{20}$ samples doped with 30 ppm of boron were determined from EBSD maps as a function of the employed annealing temperatures. Analysis of the fitted grain size data versus the different annealing temperatures (Fig. 4(a)) reveals two trends concerning the influence of boron on the grain size: i) the higher the temperature, the larger is the grain size; ii) although boron doping has a relatively small effect on the grain size for samples with grain sizes below 3.5 μm (annealed at temperatures below 800 °C), the effect becomes much more pronounced in samples with coarser grains (annealed at temperatures above 800 °C).

Based on the current work and earlier findings [30,31], boron
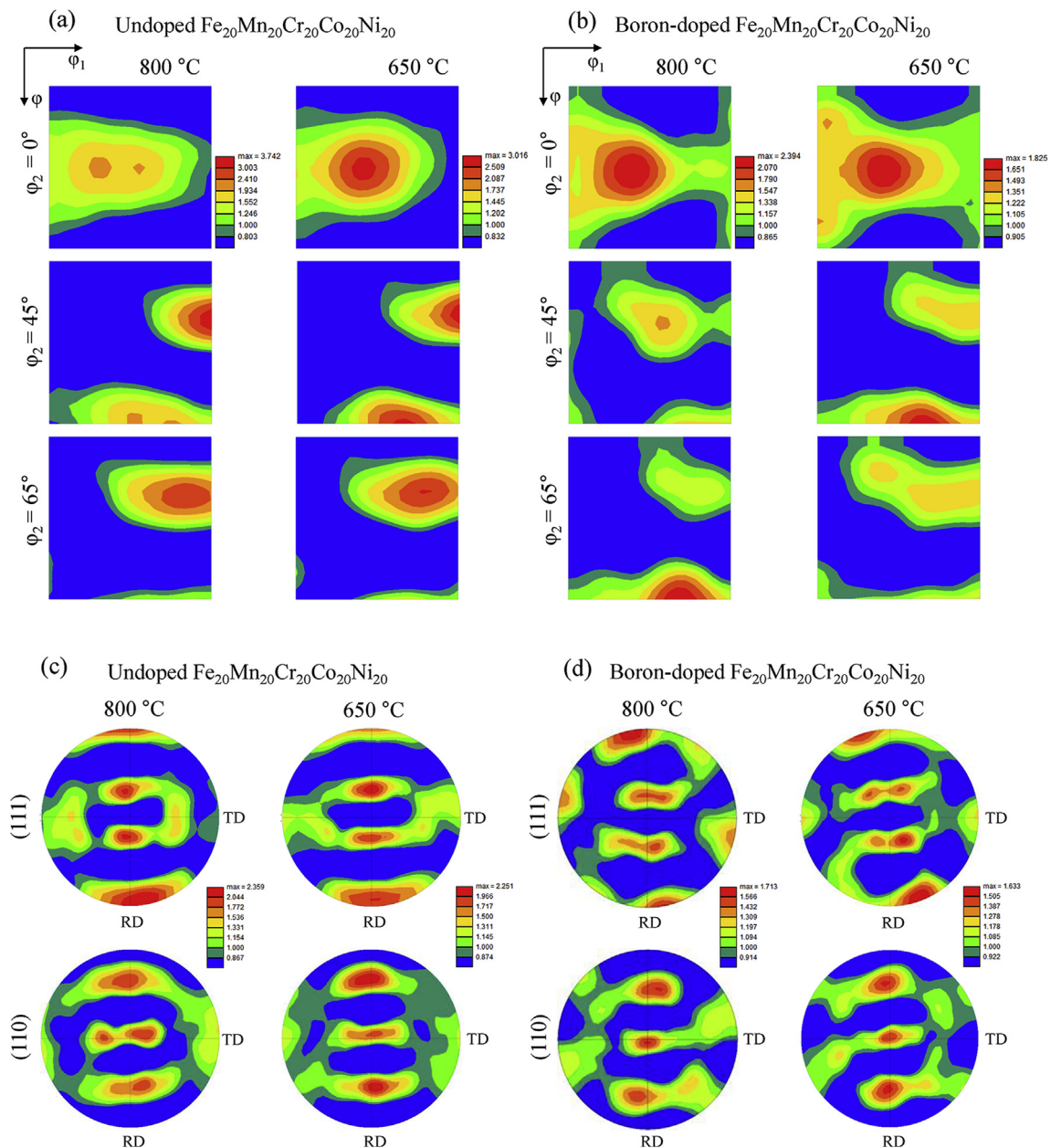
Fig. 5. Orientation distribution functions (ODFs) in Euler space and pole figures (PFs) for the (a and c) undoped $Fe_{20}Mn_{20}Cr_{20}Co_{20}Ni_{20}$ and (b and d) boron-doped $Fe_{20}Mn_{20}Cr_{20}Co_{20}Ni_{20}$ samples subjected to annealing at 800 °C and 650 °C, respectively.

doping (30 ppm) effects on the grain growth kinetics were estimated. The data were fitted by classical mean-field grain growth kinetics, where the mean grain size and annealing time are related by the following equation [32].

$$D^n_m - D^n_0 = C \times t \qquad (1)$$

where D_m is the measured mean grain size, D_0 is the initial grain size (here, D_0 is chosen to be 1 μm [30]), C is a constant, which depends on the temperature and bulk alloy composition, t is the annealing time, and n is the kinetic coefficient quantifying the grain growth behavior. The kinetic constant C for grain growth of the boron-doped and undoped equiatomic HEA samples subjected to annealing at different temperatures between 650 and 1100 °C assumes an Arrhenius form [33].

$$C = C_0 \times \exp(-Q/RT) \qquad (2)$$

where C_0 is a pre-exponential factor, Q is the activation energy for grain growth, R is the gas constant, and T is the annealing temperature. Hence, the Q value can be determined from the plot of ln $\{(D^n_f - D^n_0)/t\}$ against the reciprocal of the annealing temperature (1/T), where $D_f = 9/8 D_m$ (D_m, the measured mean grain size) is the final grain size [31].

In classical grain growth theory, the value of grain growth exponent n for the annealed metals is typically in the range of 2 (for a uniform grain growth process) to 4 (for a non-uniform or abnormal grain growth process) [34]. Also, the n value is generally provided by a double-logarithmic plot of grain sizes as a function of

heat treatment time for the materials [30]. Due to a lack of experimental results on grain size variation with annealing time, all the n values were ranged from 2.0 to 4.0 (Fig. 4 (b) and Fig. 4(c)). The data points for both equiatomic alloys (i.e. with and without boron) are not linear as a function of annealing temperature for all the grain growth exponent considered. Taking into account both the microstructural observations of non-uniform coarsening above 800 °C (Fig. 3) and the retardation of grain growth due to the presence of boron (Fig. 4(a)), we determined the best-matching fitting values of the grain growth exponent n, which were approximately 3.0 [30] for the undoped samples and approximately 3.75 for the boron-doped samples, when calculating the Q values. With the fitted values for the grain growth exponent n, the activation energies Q for both, the boron doped and undoped samples were calculated separately for two temperature regimes, i.e. 650–800 °C (low temperature regime, LT) and 800–1100 °C (high temperature regime, HT), i.e. Q_{LT} and Q_{HT}, respectively, Fig. 4(d). The resulting values for Q_{LT} and Q_{HT} were found to be 227 and 331 kJ/mol, respectively, for the undoped equiatomic HEA, and $Q_{LT} = 212$ kJ/mol and $Q_{HT} = 405$ kJ/mol for the boron-doped equiatomic samples. The drastic increase in activation energies at high temperatures upon boron doping documents its high efficiency in hampering grain coarsening kinetics. On the contrary, the difference in activation energies at low temperatures was not significant, because lattice diffusion instead of GB migration might be the prevalent mechanism The reason why a pronounced difference in activation energy only exists at high temperatures could be due to the high power index of $n = 3.75$ that was fitted for the boron-doped samples. In fact, a high value of the index n (Fig. 4(c)), as observed for the
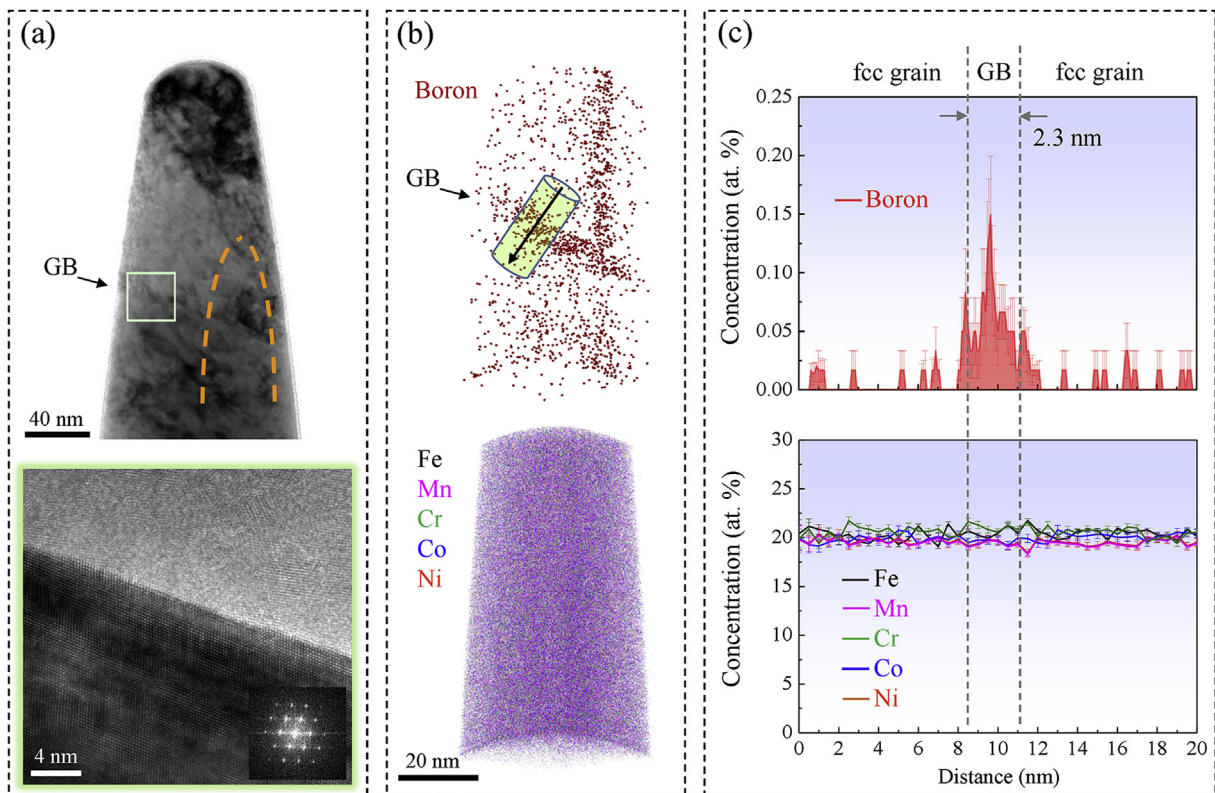
Fig. 6. Correlative analysis of the location of boron in the boron-doped (30 ppm) equiatomic Fe20Mn20Cr20Co20Ni20 HEA when subjected to 650 °C annealing: (a) Bright-field TEM image of an APT tip taken from a region containing high-angle GBs and the corresponding high-resolution TEM (HRTEM) image from the rectangle outlined; (b) APT reconstructions from the same TEM-observed tip shown in (a). The TEM images show tips prior to APT analysis, which were further sharpened after HRTEM analysis to remove any electron-induced damage layers on the tip surfaces. (c) 1D concentration profiles across the TEM/APT-observed GBs along the arrow integrating over the cylinder cross section as indicated in the APT reconstruction (b). Error bars in (c) represent 2σ measurements. APT, atom probe tomography; GB, grain boundary; TEM, transmission electron microscopy.

boron-doped samples, indicates slow grain coarsening kinetics resulting from the solute-drag effect that boron exerts on the boundaries. The Q_{HT} value of 331 kJ/mol observed for the undoped samples is similar to that reported in an earlier study [30], where a value of $Q_{HT} = 322$ kJ/mol was observed.

For studying the crystallographic recrystallization texture forming under the effect of boron doping, we analysed all EBSD data obtained from the boron-free and boron-doped $Fe_{20}Mn_{20}Cr_{20}Co_{20}Ni_{20}$ alloys subjected to annealing at 800 and 650 °C for 60 min, respectively. From pole figures (PFs) and orientation distribution functions (ODFs) plotted in Euler space the recrystallization textures were analysed. We found that the characteristic rolling texture components were reduced during recrystallization similar to the texture evolution known in twinning-induced-plasticity (TWIP) steels with low stacking fault energy (SFE) [35]. Details of the recrystallization texture components and their evolution during recrystallization of an undoped equiatomic $Fe_{20}Mn_{20}Cr_{20}Co_{20}Ni_{20}$ alloy have been described in an earlier work of Bhattacharjee et al. [35] who reported no preferred texture evolution during recrystallization of the boron-free $Fe_{20}Mn_{20}Cr_{20}Co_{20}Ni_{20}$ Cantor alloy. As shown in Fig. 5, the PFs and ODFs of both, the undoped and the boron-doped (30 ppm) $Fe_{20}Mn_{20}Cr_{20}Co_{20}Ni_{20}$ alloys in the recrystallized state (i.e. annealed at 800 and 650 °C)

reveal that the recrystallization texture consists of an incomplete <011>//normal direction α-fiber, {112}<111> Cu and {123}<634> S components. The α-fiber extends along the {110}<100> Goss to the {110}<110> 90° rotated Goss through the {110}<112> Bs component. This finding reveals no significant differences in the recrystallization textures between the undoped and the boron-doped (30 ppm) HEAs.

3.2.2. Grain boundary segregation revealed for individual boron atoms

To reveal the exact location of boron with the aim to test our hypothesis that it acts through GB segregation and the associated solute drag effect, we conducted a correlative analysis using TEM and APT [36] on the boron-doped (30 ppm) equiatomic $Fe_{20}Mn_{20}Cr_{20}Co_{20}Ni_{20}$ samples in recrystallized state. For the 650 °C annealed specimen (grain size of approx. 1.8 μm), random high angle GBs were imaged using high-resolution TEM, Fig. 6(a), and cross-correlated with the boron decoration observed by APT, Fig. 6(b). The TEM images show one APT tip prior to APT analysis, which were further sharpened after HRTEM observation to remove any electron-induced damage layers on the tip surfaces. These results reveal that the boron is located at the GBs. Such boron decoration behavior, demonstrated in the 650 °C annealed specimen,
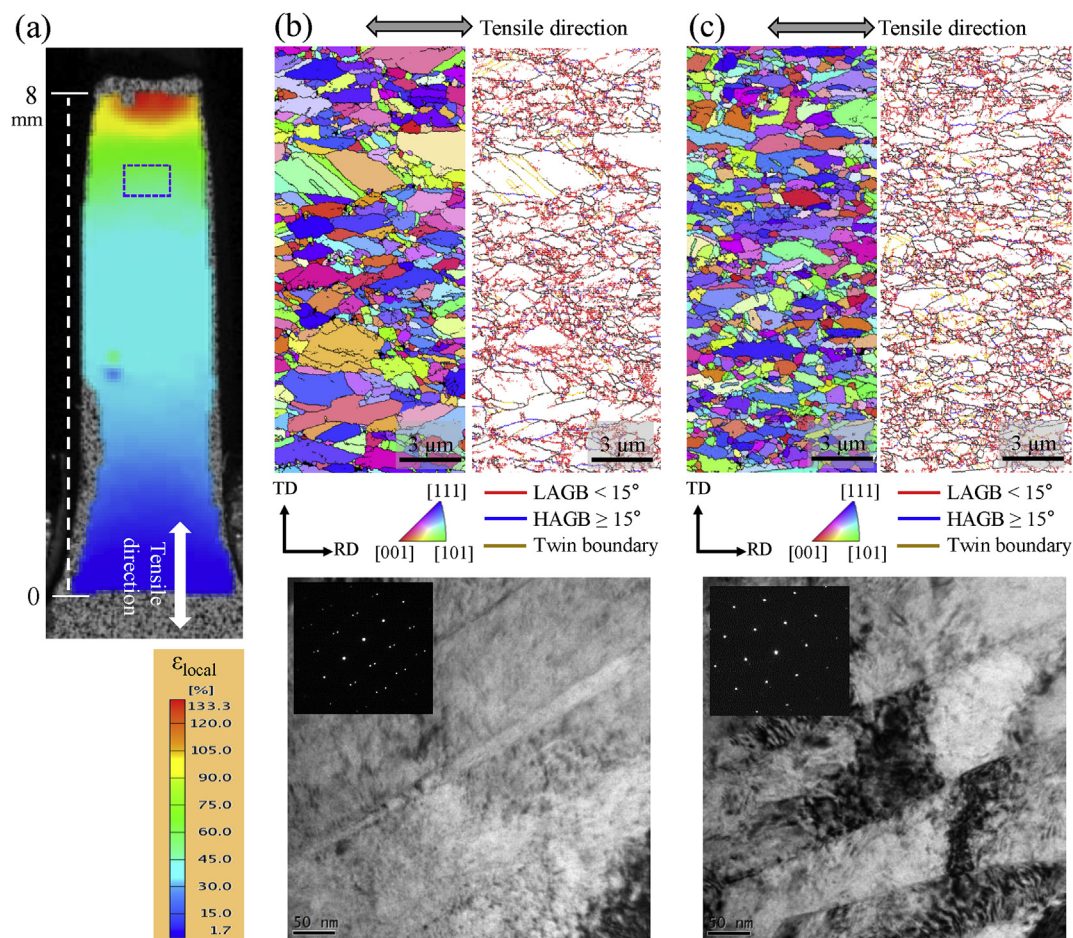
Fig. 7. (a) Representative strain distribution map of the tensile-tested $Fe_{20}Mn_{20}Cr_{20}Co_{20}Ni_{20}$ HEA samples with 30 ppm boron doping. The EBSD results (IPF maps and misorientation maps) and TEM micrographs, taken from the region subjected to a local strain level of ~70% (marked region in (a)), of (b) undoped $Fe_{20}Mn_{20}Cr_{20}Co_{20}Ni_{20}$ sample subject to annealing at 800 °C and (c) boron-doped (30 ppm) $Fe_{20}Mn_{20}Cr_{20}Co_{20}Ni_{20}$ sample subject to the same annealing. Strain distribution maps are obtained from digital image correlation (DIC). The distance of sample position from the fractured surface of each sample is displayed as 0—8 mm in DIC maps. The misorientation angle maps reveal the formation of mechanical twins (red) in the highly deformed microstructures of both the boron-doped and the undoped equiatomic samples. IPF, inverse pole figure; LAGB, low angle grain boundary with a misorientation angle <15°; HAGB, high angle grain boundary with a misorientation angle ≥15°. (For interpretation of the references to color in this figure legend, the reader is referred to the Web version of this article.)

was also observed in the 800 °C annealed sample (grain size of ~3.4 μm), Supplementary Information Fig. S4. The 1D concentration profiles probed across the TEM-mapped GBs by APT revealed that for both, the 650 °C and the 800 °C annealed samples, the boron concentration reaches the respective maximum values of ~0.15 and ~0.18 (at%) at the GBs (see Fig. 6 and Supplementary Information Fig. S4). Inside the adjacent grains, the boron concentration was found to be below the detection limit. The principal substitutional alloying elements Fe, Mn, Cr, Co and Ni were randomly distributed in both the 650 °C and the 800 °C annealed samples, as confirmed by the 1D concentration profiles and the statistical binomial frequency distribution analysis taken from the matrix phase, Supplementary Information Fig. S5. This observation suggests that substitutional solid solution strengthening in the equiatomic HEA acts independent of the presence of boron.

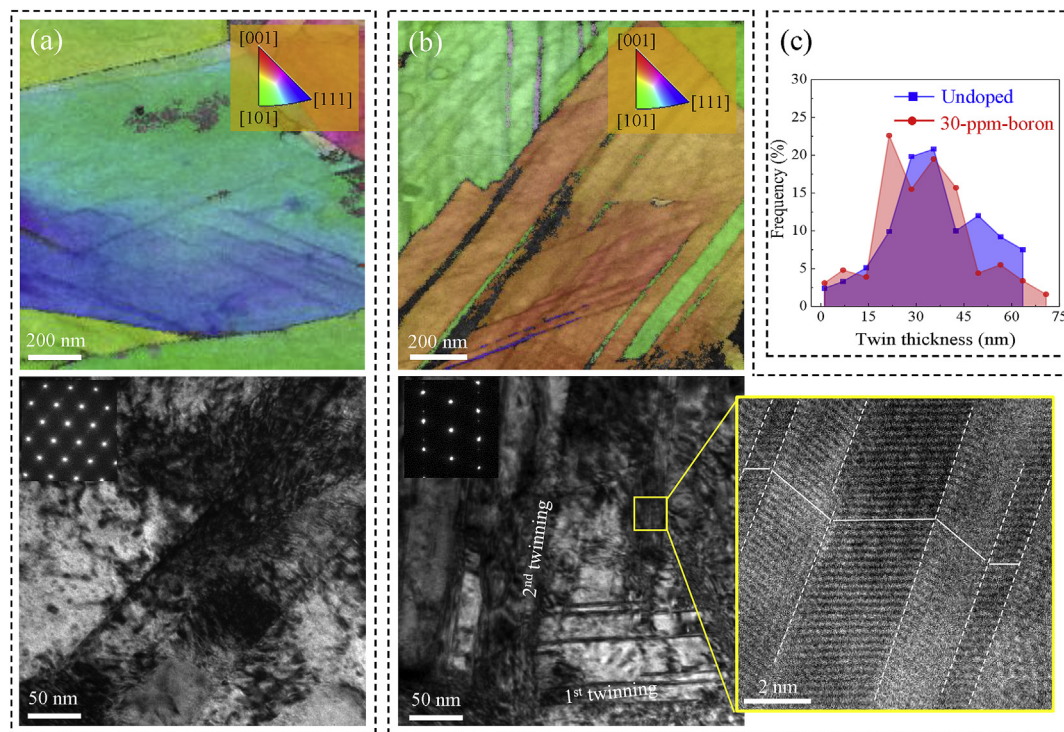### 3.2.3. Deformation microstructures

To observe the deformation structures of the boron-doped (30 ppm) and undoped HEAs, we performed EBSD and TEM probing on the $Fe_{20}Mn_{20}Cr_{20}Co_{20}Ni_{20}$ samples in regions subjected to a local strain level of ~70%. Fig. 7 shows (i) the representative strain distribution map, obtained from DIC (Fig. 7(a)) within the tensile-tested $Fe_{20}Mn_{20}Cr_{20}Co_{20}Ni_{20}$ HEA samples, (ii) the corresponding EBSD grain orientation maps and misorientation angle maps, and (iii) the corresponding TEM micrographs and SADP for the undoped (Fig. 7(b)) and boron-doped samples (Fig. 7(c)), taken from the marked region in Fig. 7(a). The deformation microstructures, obtained from EBSD and TEM, demonstrate that mechanical twinning occurred in the equiatomic HEA for both, the boron-doped and undoped equiatomic FeMnCrCoNi tensile-tested samples at such high deformation. Similar populations of mechanical twins were found in both types of samples in the deformed state which indicates that the boron does not profoundly affect the stacking fault

energy or the twin nucleation mechanism.

Further characterization by TKD, TEM, and HRTEM was performed on the DIC-tensile tested $Fe_{40}Mn_{40}Cr_{10}Co_{10}$ materials at a local strain level of ~70%, Fig. 8. In the deformed microstructure of the undoped and boron-doped FeMnCrCo HEAs (Fig. 8(a) and (b)), primary and secondary twins were observed in the EBSD maps and TEM micrographs. We further observed that the boron-doped sample has a similar twin thickness distribution as the undoped sample, Fig. 8(c).

4. Discussion

Upon boron doping, no noticeable changes were observed in the deformation structures of both the equiatomic $Fe_{20}Mn_{20}Cr_{20}Co_{20}Ni_{20}$ (Fig. 7) and the non-equiatomic $Fe_{40}Mn_{40}Cr_{10}Co_{10}$ (Fig. 8) HEAs. This result is consistent with the strain hardening response with respect to boron doping, Fig. 9, i.e. boron doping with 30 ppm did also not profoundly affect strain hardening in either the equiatomic $Fe_{20}Mn_{20}Cr_{20}Co_{20}Ni_{20}$ (annealed at 800 and 650 °C) or the non-equiatomic $Fe_{40}Mn_{40}Cr_{10}Co_{10}$ (annealed at 800 °C) HEAs. These observations suggest that the prevalent deformation mechanism in each sample type remains unaffected by boron doping with 30 ppm, thereby explaining, both improved strength and ductility of the HEA materials. In the non-equiatomic material, twinning-induced plasticity (TWIP) was the predominant deformation mechanism owing to the reduced stacking fault energy [11,12]. In the equiatomic FeMnCrCoNi alloy, dislocation strain hardening and some mechanical twinning occurred [10,37]. Hence, the strength gain observed in both materials, i.e. the boron-doped equiatomic and non-equiatomic alloys, relative to the undoped samples are attributed to the effects that boron has through its accumulation on the GBs as discussed above and not to changes in the bulk strain hardening mechanism. This conclusion suggests

Fig. 8. Deformation microstructures of the tensile-tested non-equiatomic $Fe_{40}Mn_{40}Cr_{10}Co_{10}$ samples under externally applied tensile loads until a local strain of ~70% for (a) undoped sample, as revealed by a combined TKD (upper image) and TEM (lower image) analysis, and for (b) boron-doped (30 ppm) sample, as revealed by a joint TKD, TEM and HRTEM (lower right) analysis. (c) Lamellar twin thickness distribution of the two samples, determined from TKD and TEM images. TKD: transmission Kikuchi diffraction.

(a)

(b)
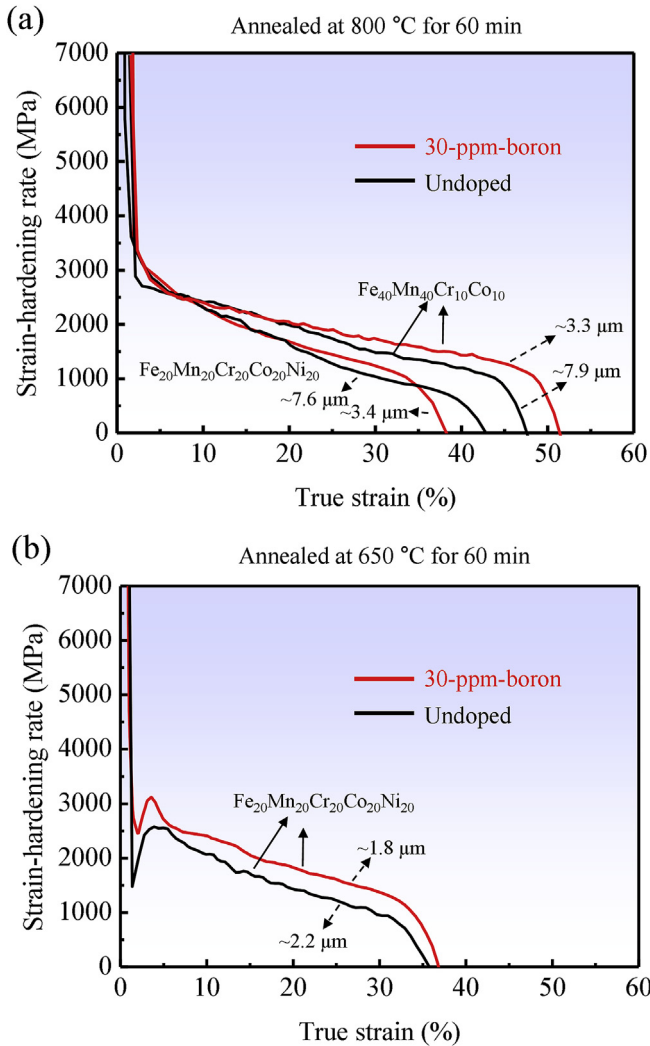
Fig. 9. Strain-hardening response of the equiatomic $Fe_{20}Mn_{20}Cr_{20}Co_{20}Ni_{20}$ and non-equiatomic $Fe_{40}Mn_{40}Cr_{10}Co_{10}$ HEAs in the recrystallized state: (a) boron-doped (30 ppm, red) and undoped (black) samples subject to annealing at 800 °C; (b) boron-doped and undoped equiatomic samples subject to annealing at 650 °C. Also included in (a) are the non-equiatomic samples subject to the same annealing (800 °C). Grain sizes (dotted arrows) of all recrystallized samples are in micrometres. (For interpretation of the references to color in this figure legend, the reader is referred to the Web version of this article.)

that boron doping should work in a similar way also for other HEAs.

Considering the Hall-Petch relation of the annealed $Fe_{20}Mn_{20}Cr_{20}Co_{20}Ni_{20}$ alloys at 800, 1000 or 1150 °C, as proposed in an earlier study [10], we recognized that the YS value of the current boron-free and boron-doped (30 ppm) $Fe_{20}Mn_{20}Cr_{20}Co_{20}Ni_{20}$ alloys (annealed at 650 °C) were unexpectedly high (Fig. 1(b)). We attribute this finding to the fact that the boron-free and boron-doped $Fe_{20}Mn_{20}Cr_{20}Co_{20}Ni_{20}$ materials were partially recrystallized only upon annealing at 650 °C for 60 min. More specific, according to the current EBSD measurements, the recrystallized fractions of the boron-free and boron-doped (30 ppm) $Fe_{20}Mn_{20}Cr_{20}Co_{20}Ni_{20}$ alloys, when annealed at 650 °C, were ~90% and ~83%, respectively. Recently, it was reported that partial recrystallization in 650 °C annealed $Fe_{20}Mn_{20}Cr_{20}Co_{20}Ni_{20}$ HEA materials can affect YS values due to the high remaining density of stored dislocations in the unrecrystallized grains [29].

GB strengthening σ_{GB} in metals can be calculated according to $\sigma_{GB} = K/\sqrt{d}$, where K is a composition-dependent Hall-Petch

constant, representing the GB's intrinsic resistance against transmission of the plastic deformation flux, and d is the mean grain size. In this context, boron performs threefold. (i) Kinetics: Boron creates an enormous GB drag effect as revealed by the increased activation barriers for grain coarsening thereby reducing the interface velocity and, thus, the grain size d. This effect acts on the argument of the exponential GB mobility function, i.e., it is a very strong effect already for minor doping content. Moreover, as an additional effect, boron retards recrystallization of the cold-rolled deformation microstructure as revealed by the increased activation barriers. This effect is seen only in $Fe_{20}Mn_{20}Cr_{20}Co_{20}Ni_{20}$ samples subjected to the low temperature annealing of 650 °C. (ii) Energetics: The driving force for GB decoration by boron lies in reducing the interfacial energy according to the Gibbs absorption isotherm. The reduced GB energy linearly reduces the capillary driving force for competitive grain coarsening and, thus, the grain size d. (iii) Mechanics: Solute boron may enhance the cohesion of GBs when mechanically loaded [19–26]. Yet, further studies are required to fully understand this mechanism. The aforementioned three effects lead to the improved tensile properties documented in this study. Boron segregation driven grain-size stabilization increases and eventually dominates GB strengthening. The influence of boron-induced GB strengthening is particularly efficient in fine-grained samples (grain size below 3.0 μm), where grain-size stabilization and, thus, hardening have an important contribution to the overall material strength. In samples with larger grain size, the boron-induced increase in GB cohesion gains momentum, since larger grains promote strain localization producing stress peaks at internal interfaces. For the 650 °C-annealed $Fe_{20}Mn_{20}Cr_{20}Co_{20}Ni_{20}$ samples showing partial recrystallization, 30 ppm boron doping stabilizes the grain-size, increases GB cohesion and increases the fraction of unrecrystallized grains (from 10% for undoped samples to 17% for the doped ones). These effects improve the material's strength by up to ~200 MPa at maintained ductility, as indicated by arrow 1 in Fig. 10. For the 800 °C-annealed equiatomic alloys with fully recrystallized microstructure, the joint effect of grain-size stabilization and boron-enhanced GB cohesion contributes to the strength increase owing to 30 ppm boron doping, causing a slight drop in ductility (see arrow 2 in Fig. 10). Similarly, for the non-equiatomic $Fe_{40}Mn_{40}Cr_{10}Co_{10}$ samples subjected to the same heat treatment (800 °C-annealing), the joint activity of grain-size stabilization and boron-induced GB cohesion improves both the strength and ductility (see arrow 3 in Fig. 10). Because of the difference in the underlying deformation mechanisms between the equiatomic FeMnCrCoNi and the non-equiatomic TWIP-assisted FeMnCrCo samples, the boron-induced strength increment in the equiatomic alloy exceeds that observed in the non-equiatomic HEA. This result confirms that compositional modification of GBs instead of the bulk by doping with very small concentrations of boron, especially 30 ppm, is an efficient method for attaining better mechanical properties of single-phase HEAs at room temperature.

Also, the crystallographic texture evolution during recrystallization of the HEAs was analysed to reveal possible correlations between processing and mechanical response. As we found no significant differences in the recrystallization textures between the undoped and the boron-doped $Fe_{20}Mn_{20}Cr_{20}Co_{20}Ni_{20}$ alloy variants in the recrystallized state (Fig. 5) no corresponding texture strengthening effect can be identified in the present study.

We found that the boron-doped HEAs reach the highest strengths at a boron concentration of 30 ppm among all alloys probed in the current study, Fig. 1(a). Beyond this concentration, boron doping is less effective but still yields alloys with better mechanical properties than undoped materials. The reduced properties observed for the high amounts (100 and 300 ppm) of boron doping are predominantly attributed to the formation of
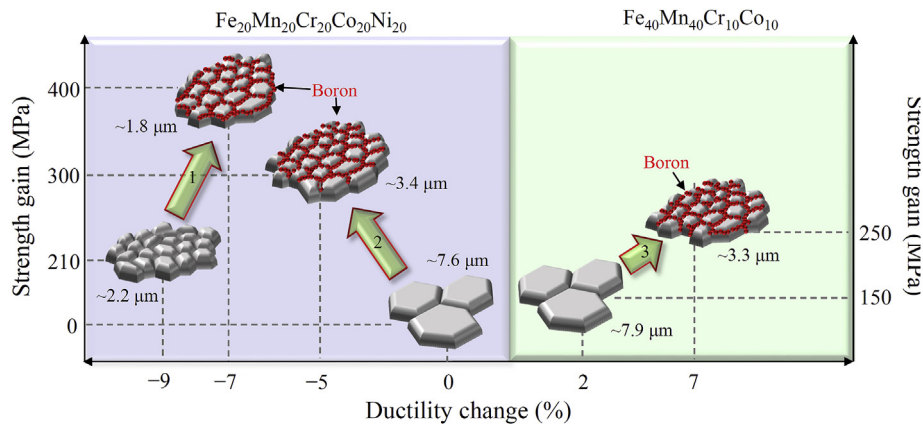
Fig. 10. Schematic of the changes of UTS and ductility (absolute levels of total tensile elongation) due to the grain size stabilization and the boron-enhanced GB cohesion. Reference state is the undoped equiatomic (grain size of 7.6 μm) sample annealed at 800 °C. Green color arrows indicate the change in tensile properties from the undoped state to the boron-doped (30 ppm) state for each HEA system: Arrow 1, for the equiatomic FeMnCrCoNi samples annealed at 650 °C; Arrow 2, for the equiatomic samples annealed at 800 °C; Arrow 3, for the non-equiatomic FeMnCrCo sample annealed at 800 °C. (For interpretation of the references to color in this figure legend, the reader is referred to the Web version of this article.)
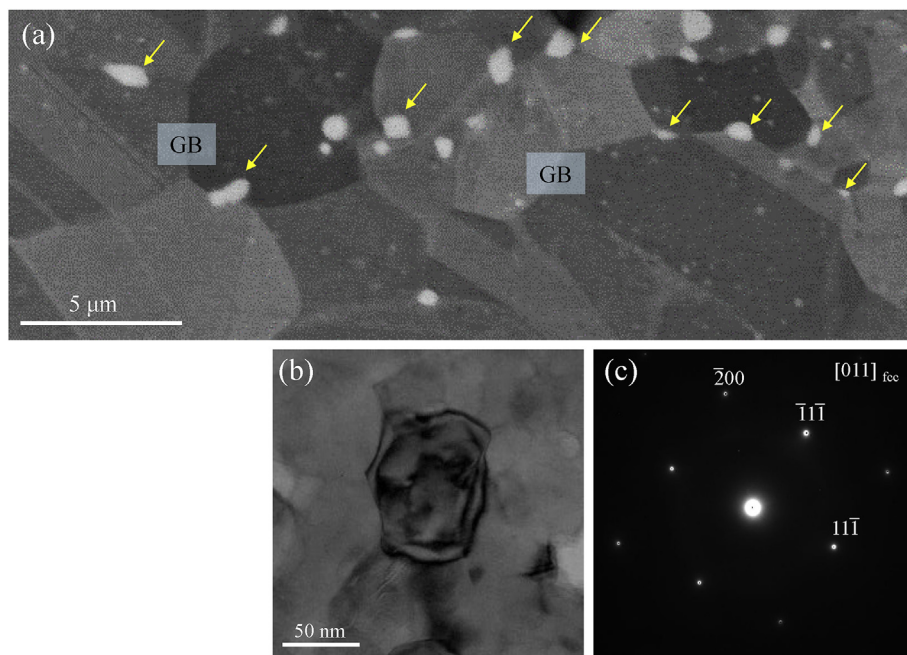
Fig. 11. (a) Representative back scattered electron micrograph of the boron-doped (300 ppm) equiatomic $Fe_{20}Mn_{20}Cr_{20}Co_{20}Ni_{20}$ sample, showing the formation of secondary compounds (bright contrast, arrows) along GBs. (b) Bright-field TEM image of a GB compound, obtained from TEM replica method, and (c) the corresponding diffraction pattern of boron-related compound with fcc crystal structure.

boron-containing compounds along the GBs, as shown in Fig. 11. These GB-compounds exhibit bright contrast in the back scattered electron (BSE) micrograph, Fig. 11(a). Also, a representative TEM micrograph, obtained through the replica method, and corresponding SADP analysis confirm the fcc crystal structure of these GB-compounds (Fig. 11(b) and (c)). Since Cr-boride (CrB) has the largest negative mixing enthalpy of -45 kJmol^{-1} among other possible binary borides such as FeB, NiB, CoB, Cr$_2$B, Fe$_2$B, Ni$_2$B and Co$_2$B [15,38], the GB-compounds that were generated in the 100- and 300-ppm-boron doped $Fe_{20}Mn_{20}Cr_{20}Co_{20}Ni_{20}$ alloys might be fcc-structured CrB borides. In accordance with an earlier works [15,39], such GB-borides thermodynamically form when the solubility limit of boron concentrations is exceeded. The borides can be so brittle that they are sufficient to initiate cracks, which might lead

to premature failure and lower ductility. These borides were not found in the 30-ppm-boron doped samples. Hence, this study confirms that 30 ppm boron doping has to be applied in the appropriate compositional range to serve as an efficient GB engineering tool for fcc-structured HEA design.

5. Conclusion

We introduce a new HEA design approach that is based on compositionally conditioning the grain boundaries instead of the bulk. GB decoration via doping with an extremely small quantity of boron enhances GB cohesion and retards capillary-driven grain coarsening leading to grain size control. As a result, as little as 30 ppm boron doping of single-phase HEAs, shown here for

equiatomic Fe$_{20}$Mn$_{20}$Cr$_{20}$Co$_{20}$Ni$_{20}$ and non-equiatomic Fe$_{40}$Mn$_{40}$Cr$_{10}$Co$_{10}$, improves their mechanical properties dramatically, increasing their yield strength by more than 100% and their ultimate tensile strength by ~40% at comparable or even better ductility. The improvement of room-temperature tensile properties demonstrate the success of the proposed GB alloying strategy for HEAs. The results show that segregation of boron at GBs is an efficient site-specific manipulation method that allows optimization of the strengths through grain size reduction and enhanced GB cohesion without sacrificing ductility. This method is also applicable to other HEAs since it improves the GB properties without affecting the bulk deformation mechanisms.

Acknowledgements

Appendix A. Supplementary data

Supplementary data related to this article can be found at https://doi.org/10.1016/j.actamat.2018.04.004.

References

[1] J.-W. Yeh, S.-K. Chen, S.-J. Lin, J.-Y. Gan, T.-S. Chin, T.-T. Shun, C.-H. Tsau, S.-Y. Chang, Nanostructured high-entropy alloys with multiple principal elements: novel alloy design concepts and outcomes, Adv. Eng. Mater. 6 (2004) 299–303.

[2] B. Gludovatz, A. Hohenwarter, D. Catoor, E.H. Chang, E.P. George, R.O. Ritchie, A fracture-resistant high-entropy alloy for cryogenic applications, Science 345 (2014) 1153–1158.

[3] B. Gludovatz, A. Hohenwarter, K.V.S. Thuston, H. Bei, Z. Wu, E.P. George, R.O. Ritchie, Exceptional damage-tolerance of a medium-entropy alloy CrCoNi at cryogenic temperatures, Nat. Commun. 7 (2016), 10602.

[4] F. Otto, Y. Yang, H. Bei, E.P. George, Relative effects of enthalpy and entropy on the phase stability of equiatomic high-entropy alloys, Acta Mater. 61 (2013) 2628–2638.

[5] D.B. Miracle, O.N. Senkov, A critical review of high entropy alloys and related concepts, Acta Mater. 122 (2017) 448–511.

[6] D.B. Miracle, B. Majumdar, K. Wertz, S. Gorsse, New strategies and tests to accelerate discovery and development of multi-principal element structural alloys, Scripta Mater. 127 (2017) 195–200.

[7] O.N. Senkov, G.B. Wilks, D.B. Miracle, C.P. Chuang, P.K. Liaw, Refractory high-entropy alloys, Intermetallics 18 (2010) 1758–1765.

[8] B. Schuh, F. Mendez-Martin, B. Volker, E.P. George, H. Clemens, R. Pippan, A. Hohenwarter, Mechanical properties, microstructure and thermal stability of a nanocrystalline CoCrFeMnNi high-entropy alloy after severe plastic deformation, Acta Mater. 96 (2015) 258–268.

[9] J.Y. He, W.H. Liu, H. Wang, Y. Wu, X.J. Liu, T.G. Nieh, Z.P. Lu, Effects of Al addition on structural evolution and tensile properties of the FeCoNiCrMn high-entropy alloy system, Acta Mater. 62 (2014) 105–113.

[10] F. Otto, A. Dlouhy, Ch Somsen, H. Bei, G. Eggeler, E.P. George, The influences of temperature and microstructure on the tensile properties of a CoCrFeMnNi high-entropy alloy, Acta Mater. 61 (2013) 5743–5755.

[11] M.J. Yao, K.G. Pradeep, C.C. Tasan, D. Raabe, A novel, single phase, non-equiatomic FeMnNiCoCr high-entropy alloy with exceptional phase stability and tensile ductility, Scripta Mater. 72–73 (2014) 5–8.

[12] C.C. Tasan, Y. Deng, K.G. Pradeep, M.J. Yao, H. Springer, D. Raabe, Composition dependence of phase stability, deformation mechanisms, and mechanical Properties of the CoCrFeMnNi High-Entropy Alloy System, JOM (J. Occup. Med.) 66 (2014) 1993–2001.

[13] Z. Li, K.G. Pradeep, Y. Deng, D. Raabe, C.C. Tasan, Metastable high-entropy dual-phase alloys overcome the strength–ductility trade-off, Nature 534

[14] J.Y. He, H. Wang, H.L. Huang, X.D. Xu, M.W. Chen, Y. Wu, X.J. Liu, T.G. Nieh, K. An, Z.P. Lu, A precipitation-hardened high-entropy alloy with outstanding tensile properties, Acta Mater. 102 (2016) 187–196.

[15] C.-Y. Hsu, J.-W. Yeh, S.-K. Chen, T.-T. Shun, Wear resistance and high-temperature compression strength of fcc CuCoNiCrAl$_{0.5}$Fe alloy with boron addition, Metall. Mater. Trans. 35 (2004) 1465–1469.

[16] W.H. Liu, Z.P. Lu, J.Y. Je, J.H. Luan, Z.J. Wang, B. Liu, Y. Liu, M.W. Chen, C.T. Liu, Ductile CoCrFeNiMo$_x$ high entropy alloys strengthened by hard intermetallic phases, Acta Mater. 116 (2016) 332–342.

[17] K. Ming, X. Bi, J. Wang, Precipitation strengthening of ductile Cr$_{15}$Fe$_{20}$Co$_{35}$Ni$_{20}$Mo$_{10}$ alloys, Scripta Mater. 137 (2017) 88–93.

[18] Y. Deng, C.C. Tasan, K.G. Pradeep, H. Springer, A. Kostka, D. Raabe, Design of a twinning-induced plasticity high entropy alloy, Acta Mater. 94 (2015) 124–133.

[19] M.P. Seah, Adsorption-induced interface decohesion, Acta Metall. 28 (1980) 955–962.

[20] C.T. Liu, C. L White, J.A Horton, Effect of boron on grain-boundaries in Ni$_3$Al, Acta Metall. 33 (1985) 213–229.

[21] M.A. Crimp, K. Vedula, Effect of boron on the tensile properties of B2 FeAl, Mater. Sci. Eng. 78 (1986) 193–200.

[22] S.P. Chen, A.F. Voter, D.J. Srolovitz, Computer simulation of grain boundaries in Ni$_3$Al: the effect of grain boundary composition, Scripta Metall. 20 (1986) 1389–1394.

[23] R. Wu, A.J. Freeman, G.B. Olson, First principles determination of the effects of phosphorus and boron on iron grain boundary cohesion, Science 15 (1994) 376–380.

[24] C.T. Liu, E.P. George, W.C. Oliver, Grain-boundary fracture and boron effect in Ni$_3$Si alloys, Intermetallics 4 (1996) 77–83.

[25] P. Lejček, S. Hofmann, V. Paidar, Segregation based classification of [100] tilt grain boundaries in α-iron and its consequences for grain boundary engineering, Acta Mater. 51 (2003) 3951–3963.

[26] D. Raabe, M. Herbig, S. Sandlobes, Y. Li, D. Tytko, M. Kuzmina, D. Ponge, P.-P. Choi, Grain boundary segregation engineering in metallic alloys: a pathway to the design of interfaces, Curr. Opin. Solid State Mater. Sci. 18 (2014) 253–261.

[27] D.P. Field, L.T. Bradford, M.M. Nowell, T.M. Lillo, The role of annealing twins during recrystallization of Cu, Acta Mater. 55 (2007) 4233–4241.

[28] Z. Wang, I. Baker, Z. Cai, S. Chen, J.D. Poplawsky, W. Guo, The effect of interstitial carbon on the mechanical properties and dislocation substructure evolution in Fe$_{40.4}$Ni$_{11.3}$Mn$_{34.8}$Al$_{7.5}$Cr$_6$ high entropy alloys, Acta Mater. 120 (2016) 228–239.

[29] J.W. Bae, J. Moon, M.J. Jang, D. Yim, D. Kim, S. Lee, H.S. Kim, Trade-off between tensile property and formability by partial recrystallization of CrMnFeCoNi high-entropy alloy, Mater. Sci. Eng. 703 (2017) 324–330.

[30] W.H. Liu, Y. Wu, J.Y. He, T.G. Nieh, Z.P. Lu, Grain growth and the Hall-Petch relationship in a high-entropy FeCrNiCoMn alloy, Scripta Mater. 68 (2013) 526–529.

[31] H. Adrian, B. Pickering, Effect of titanium additions on austenite grain growth kinetics of medium carbon V-Nb steels containing 0.008-0.018%N, Mater. Sci. Technol. 7 (1991) 176–182.

[32] P.A. Beck, J.C. Kremer, L.H. Pemer, M.L. Holzworth, Grain growth in high-purity aluminum and in an aluminum-magnesium alloy, Trans. Am. Inst. Min. Metall. Eng. 175 (1948) 372–400.

[33] J.E. Burke, D. Turnbull, Recrystallization and grain growth, Prog. Met. Phys. 3 (1952) 220–244.

[34] H.V. Atkinson, Theories of normal grain growth in pure single phase systems, Acta Metall. 36 (1988) 469–491.

[35] P.P. Bhattacharjee, G.D. Sathiaraj, M. Zaid, J.R. Gatti, C. Lee, C.W. Tsai, J.W. Yeh, Microstructure and texture evolution during annealing of equiatomic CoCrFeMnNi high-entropy alloy, J. Alloy. Comp. 587 (2014) 544–552.

[36] B.-G. Chae, J.-B. Seol, J.-H. Song, K. Baek, S.-H. Oh, H. Hwang, C.-G. Park, Nanometer-scale phase transformation determines threshold and memory switching mechanism, Adv. Mater. 29 (2017), 1701752.

[37] G. Laplanche, A. Kostka, O.M. Horst, G. Eggeler, E.P. George, Microstructure evolution and critical stress for twinning in the CrMnFeCoNi high-entropy alloy, Acta Mater. 118 (2016) 152–163.

[38] A. Takeuchi, A. Inoue, Classification of bulk metallic glasses by atomic size difference, heat of mixing and period of constituent elements and its application to characterization of the main alloying element, Mater. Trans. 46 (2005) 2817–2829.

[39] J.B. Seol, N.S. Lim, B.H. Lee, L. Renaud, C.G. Park, Atom probe tomography and nano secondaryion mass spectroscopy investigation of the segregation of boron at austenite grain boundary in 0.5 wt.% carbon steels, Met. Mater. Int 17 (2011) 413–416.